

**Light guiding light: Nonlinear refraction in rubidium vapor**J. A. Andersen,<sup>1</sup> M. E. J. Friese,<sup>1</sup> A. G. Truscott,<sup>2</sup> Z. Ficek,<sup>1</sup> P. D. Drummond,<sup>1</sup> N. R. Heckenberg,<sup>1</sup> and H. Rubinsztein-Dunlop<sup>1</sup><sup>1</sup>*Department of Physics, The University of Queensland, Brisbane, Queensland, 4072, Australia*<sup>2</sup>*Department of Physics and Rice Quantum Institute, Rice University, Houston, Texas 77251*

(Received 3 August 2000; published 18 January 2001)

Recently there has been experimental and theoretical interest in cross-dispersion effects in rubidium vapor, which allows one beam of light to be guided by another. We present theoretical results which account for the complications created by the  $D$  line hyperfine structure of rubidium as well as the presence of the two major isotopes of rubidium. This allows the complex frequency dependence of the effects observed in our experiments to be understood and lays the foundation for future studies of nonlinear propagation.

DOI: 10.1103/PhysRevA.63.023820

PACS number(s): 42.50.Gy, 42.50.Hz, 42.65.Jx, 32.10.Dk

**I. INTRODUCTION**

There has been much recent interest in the general field of “light guiding light” where cross-dispersive effects are used to control the path of a probe field using a pump field [1–7], with the long term aim of creating an all optical switch or gate [8]. Most of this work has been done with solitons in solid or liquid media. Recently, Truscott *et al.* [1] demonstrated the guiding of a 780-nm probe beam by a Laguerre-Gaussian doughnut beam. Using an intense pump beam tuned to the  $D1$  line of rubidium (795 nm), they showed that a probe beam, detuned to the red side of the  $D2$  line (780 nm), was guided into the dark, central spot of the doughnut through rubidium vapor contained in a 10-cm-long glass cell. A blue-detuned probe beam was shown to be refracted from the central spot and out of the “waveguide” structure. Truscott *et al.* [1] used a simple theory based on a three-level “V” structure and the above described tuning arrangement to qualitatively explain their results. Kapoor and Agarwal [2] extended this theoretical work based on a three-level system, to include coherence and Doppler-broadening effects. This was done through the use of a master equation approach to describe the atoms and numerical integration to describe the propagation of the probe beam in the refractive index profile resulting from the pump beam.

Nonlinear guiding of this sort can be considered to be due to population depletion in a given level. That is to say, variations of intensity in some parts of the pump beam profile vary the population in ground states that the probe interacts with, changing the effective refractive index seen by the probe. The simple three-level theoretical picture can then be seen to be insufficient to account for the specific intricacies present in rubidium’s hyperfine structure. Spectroscopy of natural rubidium shows a 3-GHz hyperfine-structure splitting of the ground state common to the two lines for the most abundant isotope of rubidium ( $^{85}\text{Rb}$ , which makes up 72% of natural samples), and a 6-GHz splitting for the same levels of the next most common isotope,  $^{87}\text{Rb}$ . As this splitting is at least an order of magnitude greater than the linewidth of a typical laser, it is vital to appreciate that the pump field cannot be simultaneously tuned to resonance with both ground levels. The effect of different detunings on the populations of both these levels needs to be considered. There is also a significant splitting between the two upper levels of the  $D1$

line that must be considered for similar reasons. In contrast, the upper level of the  $D2$  line, while having a four-level hyperfine structure, can still be treated as a “single level” as seen by the laser, due to the small energy separation between the hyperfine-structure levels relative to the width of the laser line, especially if the probe laser is tuned entirely to one side or the other of these transitions during an experiment.

Both Truscott *et al.* and Kapoor and Agarwal assume that the intensity profile of the pump beam is unchanged throughout the entire length of the rubidium cell. However, nonlinear self-dispersion effects are easily observed in rubidium (see below). If the pump beam self-focuses or is significantly absorbed in its passage through the guiding medium, this will greatly alter the form of the waveguide “written” into the vapor with propagation distance.

In this paper we extend the theory developed in [1,2] to account for the hyperfine structure of the  $D$  lines, the presence of both major isotopes of rubidium, and the possibility of tuning both the probe and the pump relative to their respective lines. To do this we, like Kapoor and Agarwal, develop a master equation; this time for the five (rather than three) atomic energy levels of both major isotopes of rubidium, which we can solve for a steady state, accounting for Doppler shifts. This treatment gives the absorption and refractive index coefficients experienced by both the probe and the pump beams. Such a five-level system could form the basis of a more detailed investigation of the resulting waveguiding. We also report experimental results using a longer cell and different frequency regimes than those investigated by Truscott *et al.* [1]. Our present results clearly confirm the need for this extension of the theory. The measured self- and cross-action effects show a frequency dependence that cannot be explained with the simple three-level system. Furthermore, we present experimental evidence that there are large self-action effects experienced within the pump beam profile and we also demonstrate guiding using a Gaussian rather than a Gauss-Laguerre pump beam profile.

**II. THEORY**

We consider the  $D1$  and  $D2$  transitions of rubidium (Rb) atoms driven by a strong (pump) laser field and probed by another weak laser beam. The pump laser, at 795 nm, is tuned near the  $5^2S_{1/2}-5^2P_{1/2}$  transitions, while the probe

laser, at 780 nm, is tuned to the  $5^2S_{1/2}-5^2P_{3/2}$  transition. The hyperfine structure of the Rb atoms'  $D$  lines can be modeled as five-level systems composed of three upper levels  $|3\rangle, |4\rangle, |5\rangle$ , and two ground levels  $|1\rangle$  and  $|2\rangle$ , as shown in Fig. 1. The pump field of frequency  $\omega_l$  is tuned near the  $|1\rangle-|3\rangle, |4\rangle$  and  $|2\rangle-|3\rangle, |4\rangle$  transitions, whereas the probe field of frequency  $\omega_p$  is tuned near the  $|1\rangle-|5\rangle$  and  $|2\rangle-|5\rangle$  transitions. We also make the approximation that the magnetic sublevels are perfectly degenerate.

We assume that spontaneous emission occurs only from the upper states  $|5\rangle, |4\rangle$ , and  $|3\rangle$  down to the lower states  $|1\rangle$  and  $|2\rangle$  with decay rates  $\Gamma_{ij}$  ( $i=3,4,5; j=1,2$ ). In a gas of Rb atoms of a temperature of about 100 °C, collisions between the atoms are frequent and have a significant impact on the level populations. We include the collisions in the dynamics of the system as an incoherent process, which can transfer the population between the ground levels  $|1\rangle$  and  $|2\rangle$  with a rate  $\Gamma_c$ . The collisional rate  $\Gamma_c$  is taken to be roughly the same order of magnitude as the spontaneous decay rates [9].

A standard procedure [10] employing the Born and Markoff approximations for the interaction of the atoms with the vacuum field leads to a description of the dynamics of the system in terms of the master equation for the reduced density operator  $\rho$ . For the five-level system considered here, the master equation can be written as

$$\begin{aligned} \dot{\rho} = & -\frac{i}{\hbar}[H_A + H_{AL}, \rho] - \frac{1}{2} \sum_{i=3}^5 \sum_{j=1}^2 \Gamma_{ij} (\sigma_{ij} \sigma_{ji} \rho \\ & + \rho \sigma_{ij} \sigma_{ji} - 2 \sigma_{ji} \rho \sigma_{ij}) - \frac{1}{2} \sum_{m=1}^2 \sum_{n \neq m=1}^2 \Gamma_c (\sigma_{mn} \sigma_{nm} \rho \\ & + \rho \sigma_{mn} \sigma_{nm} - 2 \sigma_{nm} \rho \sigma_{mn}), \end{aligned} \quad (1)$$

where

$$H_A = \hbar \omega_{21} |2\rangle\langle 2| + \hbar \omega_{31} |3\rangle\langle 3| + \hbar \omega_{41} |4\rangle\langle 4| + \hbar \omega_{51} |5\rangle\langle 5| \quad (2)$$

is the Hamiltonian of the atom, and  $\omega_{ij}$  is the angular frequency difference between levels  $|i\rangle$  and  $|j\rangle$  (refer to Fig. 1 for level numbers). We have chosen the energies of the atomic levels such that the energy of the level  $|1\rangle$  is equal to zero and the energies of the remaining levels are positive.

The first sum term in the master equation describes spontaneous emissions of photons from the upper levels  $|i\rangle$  to the ground states  $|j\rangle$  with a rate constant  $\Gamma_{ij}$ . The second sum describes the population redistribution between the ground levels due to collisions.

The operators  $\sigma_{ij}$  are the atomic transition (or dipole) operators, defined as

$$\sigma_{ij} = |i\rangle\langle j|. \quad (3)$$

In Eq. (1),  $H_{AL}$  is the interaction Hamiltonian of the atom with the laser fields. The interaction between the atom and the two fields is taken to be an electric dipole ( $\mu$ ) interaction, which (in general) is classically given by

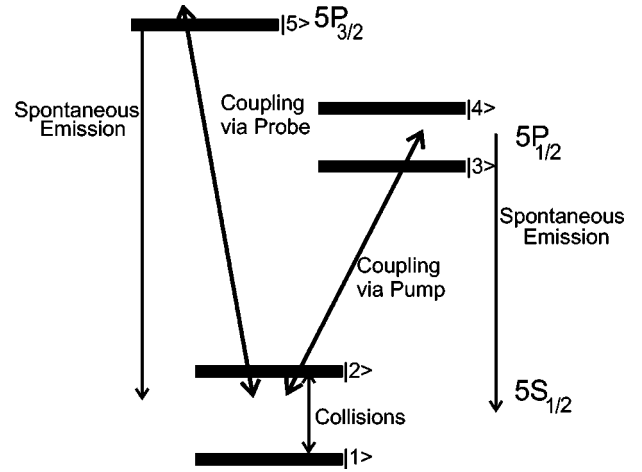


FIG. 1. Schematic diagram of the interaction model. The processes that are included are spontaneous-emission decay processes from levels  $|3\rangle, |4\rangle$ , and  $|5\rangle$  to the ground states ( $|1\rangle$  and  $|2\rangle$ ) and the absorption and/or stimulated emission transitions between the ground states and the upper states by way of the two fields, pump and probe, and also the collisional exchange between levels  $|1\rangle$  and  $|2\rangle$ . For  $^{85}\text{Rb}$ , levels  $|1\rangle$  to  $|5\rangle$  correspond to  $F=2, F=3, F=2, F=3$ , and the  $F=1$  to 4 manifold, respectively, and for  $^{87}\text{Rb}$  they correspond to  $F=1, F=2, F=1, F=2$ , and the  $F=0$  to  $F=3$  manifold.

$$H_{AL} = -\mu \cdot \mathbf{E}. \quad (4)$$

We consider  $E$ , the magnitude of the (general) laser electric field with angular frequency  $\omega$  at time  $t$  and position  $z$  propagating along the  $z$  axis, to be given by

$$E = \frac{1}{2} (E^{(+)} e^{ikz - i\omega t} - E^{(-)} e^{-(ikz - i\omega t)}). \quad (5)$$

Here,  $E^{(\pm)}$  are the positive- and negative-frequency components of the field and  $k$  is the wave number. We can ignore the spatial components from here on, by at any point shifting the origin of time so that the phase at time  $t=0$  is zero.

For the strong pump and probe laser fields, coupled respectively to the  $D1$  and  $D2$  lines, the interaction Hamiltonian can be written in the Schrödinger picture as

$$\begin{aligned} H_{AL} = & \frac{1}{2} i\hbar [(\Omega_{13}\sigma_{31} + \Omega_{14}\sigma_{41} + \Omega_{23}\sigma_{32} + \Omega_{24}\sigma_{42}) \\ & \times e^{-i\omega_l t} - \text{H.c.}] + \frac{1}{2} i\hbar [(\Omega_{15}\sigma_{51} + \Omega_{25}\sigma_{52}) \\ & \times e^{-i\omega_p t} - \text{H.c.}], \end{aligned} \quad (6)$$

where  $\Omega_{ij}$  are the Rabi frequencies of the laser fields corresponding to the allowed transitions between the atomic levels

$$\Omega_{ij} = \frac{i\mu_{ij}E^{(+)}}{\hbar} \quad (7)$$

and  $\mu_{ij}$  is the dipole moment of the transition between levels  $|i\rangle$  and  $|j\rangle$  and  $E$  is the amplitude of the field coupled to this transition.

When we ignore the hyperfine structure of the  $D$  lines (i.e., we ignore levels  $|2\rangle$  and  $|4\rangle$ ), the master equation (1) with the Hamiltonians (2) and (6) reduces to the standard master equation of a three-level  $V$ -type system considered by Truscott *et al.* [1] and Kapoor and Agarwal [2].

The master equation (1) contains all the information about the dynamics and the stationary properties of the system. We solve the master equation in terms of the density-matrix elements of the system in which the diagonal terms are the populations of the atomic levels and the off-diagonal terms are coherences (dipole moments). In the basis of the atomic levels, the reduced density operator of the system is given by

$$\rho = \sum_{i,j=1}^5 \rho_{ij} |i\rangle\langle j|, \quad (8)$$

where  $\rho_{ij}$  are the density matrix elements.

Substituting Eq. (8) into Eq. (1), we find that the master equation leads to a set of 25 coupled homogeneous differential equations for the density-matrix elements with time-dependent coefficients. We can remove the time dependence by moving the off-diagonal density-matrix elements to the following rotating frame:

$$\begin{aligned} \tilde{\rho}_{ij}(t) &= \rho_{ij} e^{i\omega_l t} \quad (i=3,4; j=1,2), \\ \tilde{\rho}_{mn}(t) &= \rho_{mn} e^{i\omega_p t} \quad (m=5; n=1,2), \end{aligned} \quad (9)$$

in which the density-matrix elements corresponding to the  $|3\rangle, |4\rangle - |2\rangle, |1\rangle$  transitions oscillate with the frequency  $\omega_l$ , and the density-matrix elements corresponding to the  $|5\rangle - |2\rangle, |1\rangle$  transitions oscillate with the frequency  $\omega_p$ . In the rotating frame (9) some of the coefficients of the differential equations still depend on time. However, the time dependence is proportional to the frequency difference  $\omega_l - \omega_p$ . Since the frequencies of the pump and probe fields are significantly different and we are interested in the stationary properties of the system, these coefficients oscillate rapidly in time and we can make the secular approximation, in which we ignore these rapidly oscillating coefficients as being small when compared to the nonoscillating terms.

Using the trace property of the density operator,  $\text{Tr}[\rho] = 1$ , the system of 25 homogeneous differential equations reduces to a closed set of 24 inhomogeneous differential equations for the density-matrix elements. For the purposes of numerical computation, it is convenient to write the set of equations in a matrix form as

$$\dot{\tilde{\rho}}_{ij}(t) = \mathcal{M} \tilde{\rho}_{ij}(t) + I, \quad (10)$$

where  $\mathcal{M}$  is the matrix of coefficients of the equations of motion, and  $I$  is a one-column matrix of inhomogeneous terms.

As the time scale over which the effects we observe is very long compared to either the optical period or lifetime of the excited states of Rb, we solve Eq. (10) for the steady

state by setting the time derivatives to zero and find the steady-state values of the density matrix elements by a numerical matrix inversion. By solving for the steady-state condition in this rotating frame, we get constant solutions for the rotating versions of the coherences corresponding to the transitions coupled to our fields. This means that, in this ‘‘steady state,’’ the actual coherences are oscillating at the frequency of the field to which they are coupled. For example,

$$\rho_{31} = \tilde{\rho}_{31} e^{-i\omega_l t} \quad (11)$$

means that  $\rho_{31}$  oscillates counterclockwise in the complex plane with amplitude  $\tilde{\rho}_{31}$  and angular frequency  $\omega_l$ .

Since the root-mean-square velocity of the Rb atoms is far from zero, and thus Doppler effects are quite clearly seen in the spectroscopy of Rb at this temperature, it is necessary to consider the Doppler shift of the light caused by the thermal motion of the atoms. This is approximated by a discrete sum over a number of velocity bins, modifying the frequency as required and weighting these contributions to the polarization by the fraction of atoms in the bins. For this work we used 15 velocity bins, each centered around velocities chosen so that the fraction of atoms in each bin was equal.

It is easy to show that if we choose to represent the velocity distribution with  $K$  velocity elements, we can choose  $K$  axial velocities  $v_i$  that form the centers of velocity bins of equal occupation, if the  $v_i$  are given by

$$v_i = -\sqrt{\frac{2kT}{M}} \text{Erf}^{(-1)}(1 - 2u_i), \quad (12)$$

where  $k$  is Boltzmann’s constant,  $T$  the temperature,  $M$  the mass of the atoms,  $\text{Erf}^{(-1)}(x)$  is the inverse of the error function  $\text{Erf}(x)$ , and the  $u_i$  are given by

$$u_i = \frac{i - \frac{1}{2}}{K}. \quad (13)$$

Then, we can easily combine the contributions to density-matrix elements from each of the 15 velocity bins

$$\rho_{mn} = \sum_{i=1}^{15} \rho_{mn}(v_i) \quad (14)$$

to get the total density matrix for the Doppler-broadened ensemble.

In order to account for the presence of the two isotopes, this master equation is solved for each of the isotopes separately then the polarizations are summed, weighted by the abundances of  $^{85}\text{Rb}$  and  $^{87}\text{Rb}$ .

Here, we are interested in the dispersive and absorptive properties of the rubidium atoms. The properties are determined by the polarization  $P$  of the atoms [11], whose average value can be written in terms of the density-matrix elements as [12]

$$\langle P \rangle = \sum_{i=1}^2 \sum_{j=3}^5 (\mu_{ij} \rho_{ji} + \text{c.c.}), \quad (15)$$

where  $\mu_{ij}$  is the dipole matrix element of the transition from level  $|i\rangle$  to  $|j\rangle$ .

The polarization  $P$  is related to the amplitude of the probe field as

$$P = \epsilon_0 \chi(\omega, E) E, \quad (16)$$

where  $\chi$  is the dielectric susceptibility of the atoms and  $\epsilon_0$  is the permittivity of free space. We assume a linear relation between the polarization ( $P$ ), dielectric susceptibility ( $\chi$ ), and the probe field amplitude ( $E$ ), but we calculate the dielectric susceptibility to all orders of a pump field intensity given by the Rabi frequency of the pump field.

In order to evaluate the refractive index of the rubidium at the frequencies of the probe field used in the experiment, we consider only those parts of the polarization that oscillate at the probe frequency. Further, just as the electric field is defined as having positive- and negative-frequency coefficients ( $E^{(+)}$  and  $E^{(-)}$ , respectively), the polarization at both the probe and pump frequencies has positive- and negative-frequency components:

$$P = \frac{1}{2} (P_p^+ e^{-i\omega_p t} + P_p^- e^{i\omega_p t} + P_l^+ e^{-i\omega_l t} + P_l^- e^{i\omega_l t}). \quad (17)$$

Therefore, in order to evaluate the dispersion parameters for the two fields, we choose one of the frequency ‘‘directions’’ and compare the electric field and polarization coefficients that correspond to that frequency and direction. For example, when the ‘‘positive-frequency’’ part of the electric field ( $E^{(+)}$ ) is compared with the positive-frequency part of the polarization, it can be shown that the susceptibility  $\chi$  is given by

$$\chi = \frac{P^{(+)}}{\epsilon_0 E^{(+)}}. \quad (18)$$

Thus the dielectric susceptibility for the fields can be calculated using Eq. (18) with the relevant polarization components of the fields [13].

To find the refractive index seen by the probe field we compare the parts of the total polarization that oscillate with the probe frequency to the probe field. When we restrict ourselves to the elements of the polarization that are oscillating at the positive probe field frequency ( $-\omega_p$ ), the polarization (15) reduces to

$$\langle P^{(+)} \rangle = \mu_{15} \tilde{\rho}_{51} + \mu_{25} \tilde{\rho}_{52}. \quad (19)$$

We can then evaluate the refractive index [ $n(\omega) = \sqrt{1 + \text{Re}(\chi)}$ ] and absorption [ $G(\omega) = \omega \text{Im}(\chi)/cn(\omega)$ ] coefficients of the gas from Eqs. (18) and (19).

Using this model, we first calculated the absorption coefficient of natural rubidium and found the general form to be in agreement with the well-known absorption spectrum. We then calculated dispersion relations, which are compared with experimental measurements of these effects.

The coherent effects mentioned in [2] are taken into account in our theoretical calculations of the refractive index.

However, the Rabi frequency of the pump field (up to 200 MHz for the powers studied here) is smaller than the 500-MHz Doppler width of the distribution; effects like Autler-Townes splitting are not seen in our results. This effect is expected to be much more prominent in cold trapped atoms, where the Doppler width can be reduced by many orders of magnitude.

### III. EXPERIMENTAL RESULTS

To examine the nonlinear effect of pumping two different atomic transitions which share a ground state, we require two laser sources. These are provided by a titanium-sapphire (Ti-S) laser with output at 795 nm (pump), and a diode laser with output at 780 nm (probe). The Ti-S laser (Coherent 899/21) is tunable near 795 nm. The laser frequency is stabilized using an external Fabry-Perot cavity, which allows the laser to be easily tuned through a range of about 20 GHz. The diode laser is frequency stabilized using grating feedback [14] and is tunable around 780 nm. Figure 2 shows a diagram of the experimental setup.

The pump and probe beams are aligned to be copropagating through the nonlinear medium. They are each independently focused so that they propagate in a collimated manner along the 40-cm rubidium cell, and are aligned with the cell entry port. A combination of the beams is achieved by first orthogonally polarizing the beams using half wave plates and then combining them at a polarizing beam splitter. The combined beams propagate through the cell containing natural rubidium vapor (72%  $^{85}\text{Rb}$  and 28%  $^{87}\text{Rb}$ ). The vapor pressure is controlled by heating the cell with a wrapping of nichrome wire with a controlled current. The temperature of the cell is measured by a digital thermometer, coupled to the cell using heat sink compound.

The output face of the heated rubidium cell is imaged onto a screen, which rotates to eliminate speckle effects in the detection. A pair of 780-nm interference filters are placed in front of this screen to block the pump light. This image is then captured by a charge-couple device (CCD) camera (Electrim) with an array of (1134 × 486) pixels and a resolution of approximately 90 pixels/mm. The frequencies of both beams are monitored with a wave meter.

In this experiment we looked at the nonlinear effects produced by both Gaussian and Laguerre-Gaussian (LG) doughnut beams. The LG beams were produced using computer-generated holograms which produce, in the far field, an  $\mathcal{L}_{03}$  mode which has a field distribution given by [15]

$$E(r, \theta) = E_0 \frac{r^3}{\omega^3} e^{-r^2/\omega^2} e^{\pm i3\theta} e^{-ikr^2/2R} e^{i(kz+4\Phi)}, \quad (20)$$

where  $\Phi$  is the Gouy phase shift and  $R$  the wave front radius of curvature. The  $e^{\pm i3\theta}$  term creates a phase singularity at the origin, leading to a dark central spot and a ‘‘doughnut’’ intensity profile.

In order to have results that can be compared easily with experiment, the refractive index variations caused by the pump are studied. This allows us to have some idea as to where self- and cross-focusing (of the pump and probe

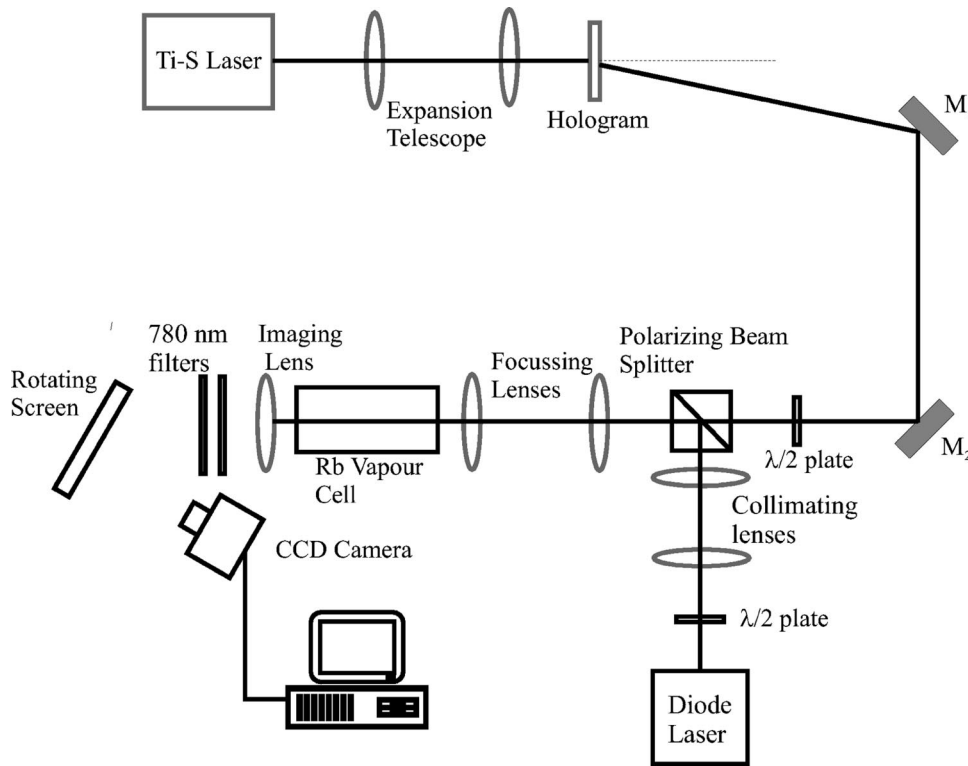


FIG. 2. Experimental arrangement for the study of nonlinear effects in the rubidium vapor cell. The hologram can be removed if a Gaussian beam is required.

beams, respectively) should occur. As the Ti-S laser spot used has intensities up to the order of  $10^5 \text{ W m}^{-2}$  within its profile, we look at the refractive index for intensities up to this value.

The variations of the pump beam refractive index with intensity and frequency (self-action effects) are studied first. In Fig. 3 we plot the variation of the refractive index at three different pump intensities. This is calculated by solving the master equation (1) as a function of pump frequency with the probe intensity set to zero and then applying Eqs. (15), (18), and (19) to the matrix elements corresponding to the pump-coupled transitions. The variation is quite complex with several peaks and troughs due to the eight transitions involved. These curves show that, firstly, the refractive index varies around unity in a shape that fits the general pattern of dispersion curves (that is, the refractive index  $n$  increases on the low-frequency side of the transition). Secondly, the magnitude of the variation of the refractive index from unity decreases with the intensity of the pump field. Thus, in a region where the variation in refractive index is positive, we have a lower refractive index in more intense regions of the beam. Then, at these frequencies, self-defocusing should occur. Conversely, we predict self-focusing in regions where the variation is negative. This decrease in the magnitude of the variation is due to the depletion of the population of the ground state with which the pump is interacting. This result clearly predicts self-defocusing when the frequency of the pump is less than approximately 377.105 THz and when the frequency of the pump is between 377.107 and 377.109 THz. Self-focusing is predicted to occur at other frequencies.

We test this prediction by imaging the beam profile of the  $\mathcal{L}_{03}$  mode in the near field, after propagation through the cell. To get an objective measure of the amount of self-focusing

or self-defocusing, we look at the change in the full width at half maximum (FWHM) of the bright ring of the doughnut. Although we certainly could use a simple Gaussian spot to test this effect, the elliptical output of the Ti-S Gaussian mode contained a number of intensity variations that led to its self-focusing into non-Gaussian shapes, which precluded

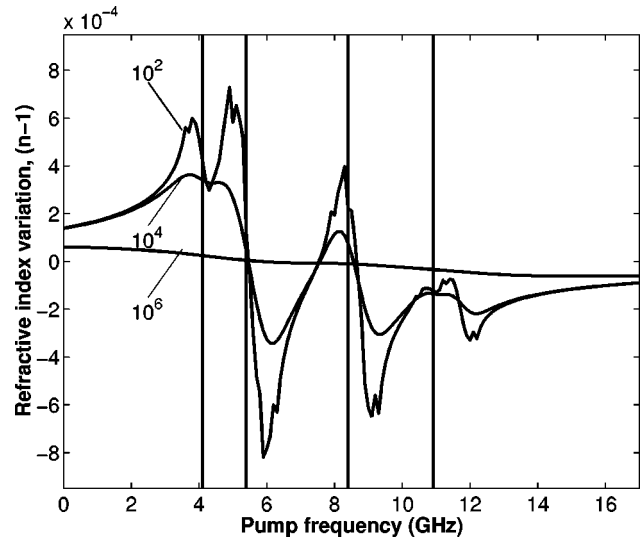


FIG. 3. Theoretical refractive index variation for rubidium near 377 THz (795 nm) at three values of pump intensity. Zero on the frequency axis corresponds to 377.1 THz. The numbers shown are pump intensities in  $\text{W m}^{-2}$  and correspond to intensities present in the beam. This variation shows the pump beams self-action effects. The vertical lines indicate the frequencies of, from left to right, the  $^{87}\text{Rb}$   $|2\rangle$  to  $|3\rangle$  transition, the  $^{85}\text{Rb}$   $|2\rangle$  to  $|3\rangle$  transition, the  $^{85}\text{Rb}$   $|1\rangle$  to  $|3\rangle$  transition, and the  $^{87}\text{Rb}$   $|1\rangle$  to  $|3\rangle$  transition.

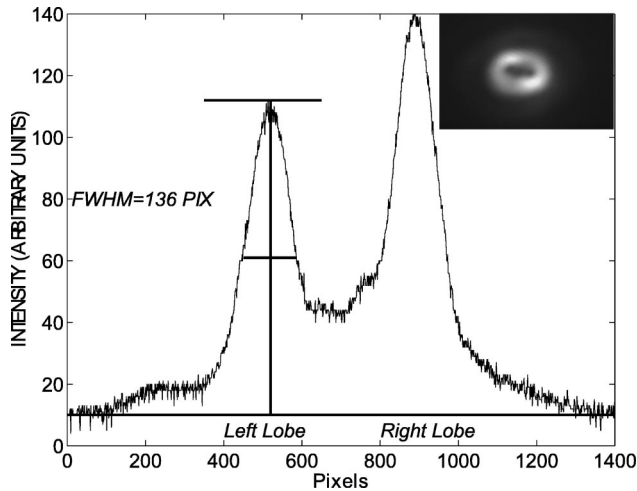


FIG. 4. Self-focusing effect: measurement of FWHM for the left lobe in the scan across row 500 of the intensity distribution for  $f=377.1070$  THz. These FWHM measurements are used to characterize the degree of self-dispersion experienced by a charge 3 Gauss-Laguerre doughnut mode in rubidium vapor (see Figs. 5 and 6). The inset shows this intensity distribution which displays self-focusing effects.

simple analysis. These shapes included stripes and spirals. However, an  $\mathcal{L}_{03}$  mode resulting from passing the elliptical Gaussian through a computer-generated hologram gave a high-quality intensity distribution that was well behaved in the nonlinear medium.

At high powers and temperatures, several very interesting effects were observed. First, the  $\mathcal{L}_{03}$  mode appeared to break up into swirling patterns of light and dark streaks that again would be impossible to easily analyze. One likely explanation for this is that any small defects in the beam are amplified by propagation in the nonlinear medium. Doughnut beams have been shown to suffer from instability under self-focusing (see, for example, [16]). The inset of Fig. 4 shows a far-field image of a charge three doughnut in such a self-focusing medium, with some evidence of breakup occurring: the bright peaks around the ring and the partial separation of the singularity. We also noticed a number of bright spots, possibly bright solitons, that formed at high temperatures ( $>70^\circ\text{C}$ ) (see, for example, [7,17]). This effect, not reported by Truscott *et al.* [1], is possibly due to the fact that the cell we used was four times longer than the one used previously, allowing nonlinearities to develop further. Due to both these effects, care was taken to keep the intensity and temperature down to values where the nonlinearities were well behaved, in the sense that they produced self-action effects that were simple to characterize and measure.

The cell was kept at a temperature of approximately  $61^\circ\text{C}$  and the pump was scanned through frequencies from 377.1000 to 377.1136 THz. This corresponds to a tuning of approximately 7 GHz to either side of the  $D_1$  line. The near-field image of the beam profile at the output face was recorded. Examples of these images are shown as insets in Figs. 4, 5, and 6.

A scan across one row of each of these images produced an intensity profile (see Fig. 4) with two peaks, correspond-

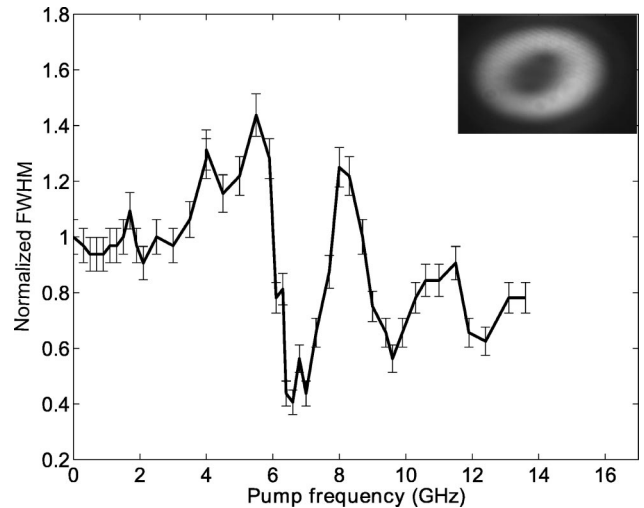


FIG. 5. Plot of relative FWHM for the left lobe (see Fig. 4) of the doughnut-profiled pump beam, normalized relative to the FWHM of the far detuned pump. Zero on the frequency axis corresponds to 377.1 THz. The inset shows the intensity distribution for 377.1 THz, which is considered “normal” and against which all other widths are normalized.

ing to the sides of the doughnut. The full widths at half maximum (FWHM) of these peaks normalized relative to the FWHM of the far detuned pump, are shown in Figs. 5 and 6.

Self-focusing will occur when the refractive index experienced by the pump is greater in regions of higher intensity. Self-focusing will lead to a narrowing of a beam, so we will have self-focusing at pump frequencies where the FWHM has decreased and the strength of the self-focusing should be characterized by the relative amount of decrease in the FWHM.

As the magnitude of the nonlinear refractive index variation decreases with increasing pump intensity, we would ex-

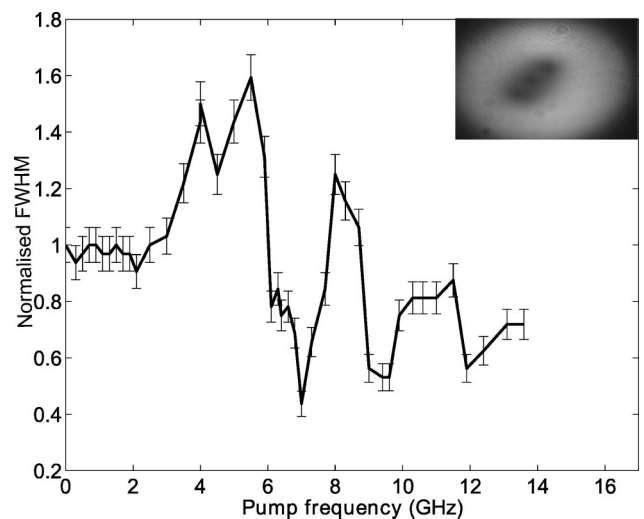


FIG. 6. Plot of relative FWHM for the right lobe (see Fig. 4) of the doughnut-profiled pump beam, normalized relative to the FWHM of the far detuned pump. Zero on the frequency axis corresponds to 377.1 THz. The inset shows the intensity distribution for pump frequency 377.1055 THz, which shows self-defocusing.

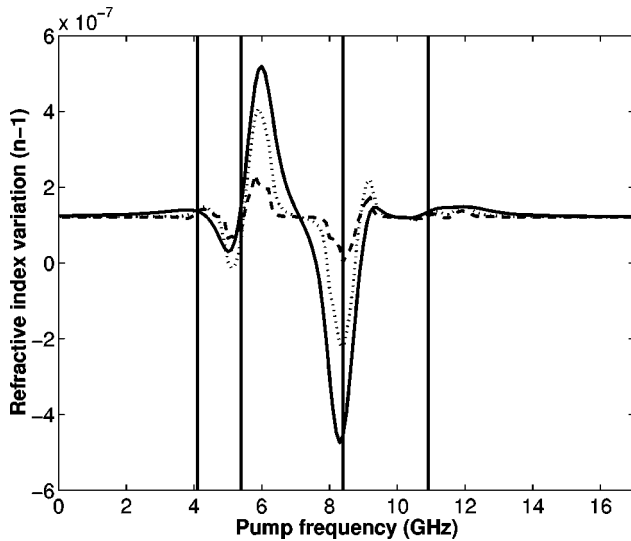


FIG. 7. Theoretical probe refractive index variation for rubidium. The frequency of the probe is 384.230 THz. Zero on the frequency axis corresponds to 377.1 THz. The vertical lines correspond to transition frequencies, as in Fig. 3. The solid, dotted, and dashed lines correspond to pump intensities of  $10^4$ ,  $10^3$ , and  $10^2$   $\text{W m}^{-2}$ , respectively.

pect that the frequencies displaying self-focusing experimentally should show a negative refractive index variation so that, where the intensity was greater, the local refractive index would be relatively higher than the surroundings. Frequencies displaying self-defocusing experimentally should show a positive refractive index variation. As can be seen (in Figs. 3, 5, and 6), this is indeed the case. In fact, as the amount of variation in the nonlinear refractive index with intensity increases with the size of the nonlinearity, the regions of strongest self-focusing and -defocusing should correspond to the largest refractive index variations, which is also the case. To calculate the influence of the pump on the probe refractive index, we again solve the master equation (1) as a function of pump frequency, but this time with a nonzero probe field. We then find the probe refractive index by applying Eqs. (15), (18), and (19) to the matrix elements corresponding to probe-coupled transitions.

The calculated probe refractive index for the probe at 384.230 THz is plotted as a function of the pump frequency in Fig. 7. It can be seen that the refractive index varies around a number greater than one (this number is the refractive index the probe would see if the pump was not present) and the size of this variation is dependent upon the pump intensity.

Thus, a probe beam at 384.230 THz, with a pump at 377.108 THz, for example, will experience a lower refractive index in regions of more intense pumping, as the nonlinearity decreases with increasing pump intensity. This means that the probe beam will be guided out of the more intense regions of the pump beam.

The probe frequency is placed between the two  $^{85}\text{Rb}$  transitions. Therefore, it is to the red (lower frequency) of the  $|1\rangle$  to  $|5\rangle$  transition and the blue (higher frequency) of the  $|2\rangle$  to  $|5\rangle$  transition (see Fig. 1). Due to this the dispersion effects

(the upwards trend in the refractive index at the red of a transition and the downwards trend at the blue) tend to cancel out somewhat. However, when the pump interacts with the ground states, it affects the populations in the two ground levels. When the pump is far off both resonances, the two states have equilibrium populations. Then, as the pump frequency is increased, it approaches the  $|2\rangle$  to  $|3,4\rangle$  resonances. This leads to a depletion in the population of ground state  $|2\rangle$  relative to ground state  $|1\rangle$ , so the probe interacts with many more atoms in the  $|1\rangle$  state than the  $|2\rangle$  state. Then, the upwards trend in the refractive index caused by interacting with an atom in the  $|1\rangle$  state has more effect on the overall refractive index, causing a rise, as seen here. Similarly, as the pump approaches the  $|1\rangle$  to  $|3,4\rangle$  resonances for  $^{85}\text{Rb}$ , the population of level  $|2\rangle$  rises relative to level  $|1\rangle$ , leading to a drop in the refractive index for the probe. Due to the far detuning of the probe from either of the  $^{87}\text{Rb}$  lines, there is little notable effect when the pump approaches the  $^{87}\text{Rb}$  resonances.

In order to demonstrate that guiding is experimentally realizable using a Gaussian pump beam profile, rather than a doughnut, a Gaussian Ti-S beam was copropagated through the cell with a probe beam from the diode laser. In contrast to the experiments of Truscott *et al.* [1], the probe beam was placed near a resonance within the rubidium  $D2$  lines near 780 nm instead of having the probe beam far detuned from all these lines, which avoids the splitting of the ground state and the isotopic makeup of natural rubidium. Due to these two isotopes present in natural rubidium, there are complications regarding tuning relative to a particular line. When one is tuned to the blue (higher frequency) of a  $^{87}\text{Rb}$  transition, say, the probe may also be tuned to the red (lower frequency) of a  $^{85}\text{Rb}$  transition, as well as having some detuning (which may be red or blue) relative to the other  $^{87}\text{Rb}$  transition. This leads to a dispersion curve with many features.

The diode laser was held at a frequency of 384.230 THz, while the pump laser was tuned through the 795-nm lines (377.0989 to 377.1165 THz). The output probe beam profiles recorded (the pump beam light was filtered out using two 10-nm bandwidth interference filters for 780 nm) are shown in Fig. 8. This figure shows the width of the Gaussian probe beam spot increasing and decreasing as the pump beam frequency is varied. When the size of the beam decreases from its regular width, it indicates that the beam is being guided within the profile of the pump beam, which reduces the expansion of the probe with propagation.

A theoretical plot of the refractive index perceived by the probe at a frequency of 384.230 THz as the pump frequency is varied is shown in Fig. 7. Pump frequencies experimentally showing cross-focusing of the probe beam into the intense regions of the pump beam should correspond to a nonlinear refractive index for the probe that increases with pump intensity; the reverse should be true for pump frequencies exhibiting cross-focusing into the dark regions of the pump. It is cross-focusing into the bright regions of the Gaussian that leads to guiding.

If we look in detail at the probe beam at different pump frequencies (Fig. 8), we can see that the probe is sometimes directed into the bright regions of the pump to form a single

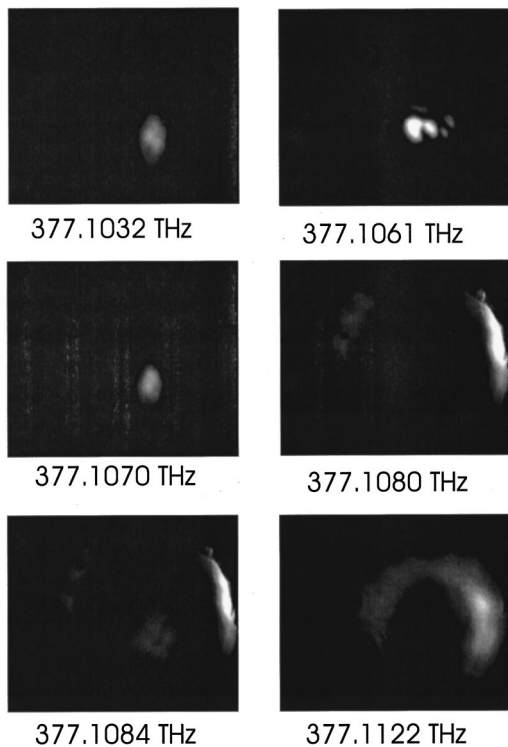


FIG. 8. Experimental measurement of guiding and antiguiding. These images show the behavior of the probe beam as the pump beam is scanned across the  $D1$  line. The images of the probe beam are taken at the output face of the cell. The frequencies shown below the images are the pump frequencies used to create these images. The probe frequency is 384.230 THz in all these images.

spot, and sometimes into the dark regions to form a bright halo. First, in the region around 377.103 THz, as Fig. 7 shows an increase in refractive index with intensity, we should see the probe beam focus into a spot, which is the case, as can be seen from the image of the probe with the pump at 377.1032 THz. Second, at 377.1061 THz, there is an even larger increase in refractive index with intensity — which leads to the tighter spot shown. Third, as the curves in Fig. 7 cross at about 377.107 THz, the direction of the intensity variation of the refractive index changes, leading to a swap from the guiding to the antiguiding regimes. The intensity profiles up to 377.107 THz show guiding while the profiles from 377.108 THz show antiguiding. Fourth, at 377.1084 THz, the decrease in refractive index as the intensity increases indicates that antiguiding behavior should occur, which is also detected. Fifth, at some frequencies, for example, around 377.1122 THz, it is difficult to see from the theoretical curves whether we should get guiding or antiguiding experimentally. In fact, at 377.1122 THz, we see some

antiguiding, which implies that, overall, the intensity profile of the pump beam must lead to a refractive index profile that refracts the beam out of the central bright spot.

It is believed that, given the success of the pump self-action results, our model should correctly reflect all the physics involved in the pump and/or probe cross-action experiments, and that cases such as the fifth one will be resolved only when a full propagation calculation is carried out.

#### IV. CONCLUSIONS

In this work a quantum-mechanical model of the interaction of rubidium atoms with two lasers tuned near the  $D1$  and  $D2$  lines was developed which takes into account the actual level structure. This model allowed predictions to be made about the dielectric polarization of the rubidium as a function of the frequency and intensity of the fields. The predicted polarization, allowed the generation of absorption spectra that matched experimental results. It was also possible to generate dispersion curves for the 795-nm (pump) beam at various intensities, which allowed a semiquantitative measure of the type and amount of self-action experienced by this beam to be predicted. These predictions were found to be in very good qualitative agreement with experimental results obtained. Further, the model was used to predict the refractive index experienced by a 780-nm (probe) beam in the presence of a strong pump beam. By investigating how this refractive index varied with pump intensity and frequency, it was possible to show a qualitative prediction of cross action, which in most cases matched the experimental observations of a weak probe interacting with an intense Gaussian pump.

In order to improve the quantitative nature of these results, it would be useful to simulate the propagation of light near the resonances in this media. The programs written in this work find the dielectric polarization of the medium as a function of the strength and frequency of the fields. This polarization term appears in Maxwell's equations for the electromagnetic field so it should, in principle, be straightforward to solve these equations numerically using these programs. When this is achieved, the accuracy of the model can be more rigorously tested by comparing the output of the simulation with the images obtained at the exit face of the cell for the same initial intensity distribution. Such propagation has been done, albeit for a simplified polarization model, by Kapoor and Agarwal [2].

The intermediate cross-dispersion results presented here allow us to deduce from a theoretical graph which frequency combinations are likely to give successful guiding before one commits to the expenditure of computational power and the time involved in a numerical propagation calculation.

[1] A. G. Truscott, M. E. J. Friese, N. R. Heckenberg, and H. Rubinsztein-Dunlop, *Phys. Rev. Lett.* **82**, 1438 (1999).

[2] R. Kapoor and G. S. Agarwal, *Phys. Rev. A* **61**, 053818 (2000).

[3] C. T. Law, X. Zhang, and G. A. Swartzlander, Jr., *Opt. Lett.* **25**, 55 (2000).

[4] G. A. Swartzlander, Jr. and C. T. Law, *Phys. Rev. Lett.* **69**, 2503 (1992).

- [5] B. Luther-Davies and X. Yang, *Opt. Lett.* **17**, 1755 (1992).
- [6] L. Poladian, A. W. Snyder, and D. J. Mitchell, *Opt. Commun.* **85**, 59 (1991).
- [7] V. Tikhonenko, J. Christou, and B. Luther-Davies, *J. Opt. Soc. Am. B* **12**, 2046 (1995).
- [8] T. Thwaites, *New Sci.* **1751**, 17 (1991).
- [9] W. Demtröder, *Laser Spectroscopy* (Springer-Verlag, Berlin, 1996).
- [10] W. H. Louisell, *Quantum Statistical Properties of Radiation* (John Wiley and Sons, New York, 1973).
- [11] A. Yariv, *Optical Electronics* (Saunders College, Philadelphia, 1991).
- [12] R. Loudon, *The Quantum Theory of Light* (Clarendon Press, Oxford, 1983).
- [13] N. Bloembergen and Y. R. Shen, *Phys. Rev.* **133**, A37 (1964).
- [14] A. G. Truscott, N. R. Heckenberg, and H. Rubinsztein-Dunlop, *Opt. Quantum Electron.* **31**, 417 (1999).
- [15] N. R. Heckenberg, R. McDuff, C. P. Smith, H. Rubinsztein-Dunlop, and M. J. Wegener, *Opt. Quantum Electron.* **24**, 5951 (1992).
- [16] D. V. Skryabin and W. Firth, *Phys. Rev. E* **58**, 3916 (1998).
- [17] B. Luther-Davies and X. Yang, *Opt. Lett.* **17**, 496 (1992).